Chapter-3

Amino acid-capped transition metal ion-doped iron oxide nanoparticles: evaluating drug delivery carrier efficiency and in vitro magnetic resonance image contrasting ability

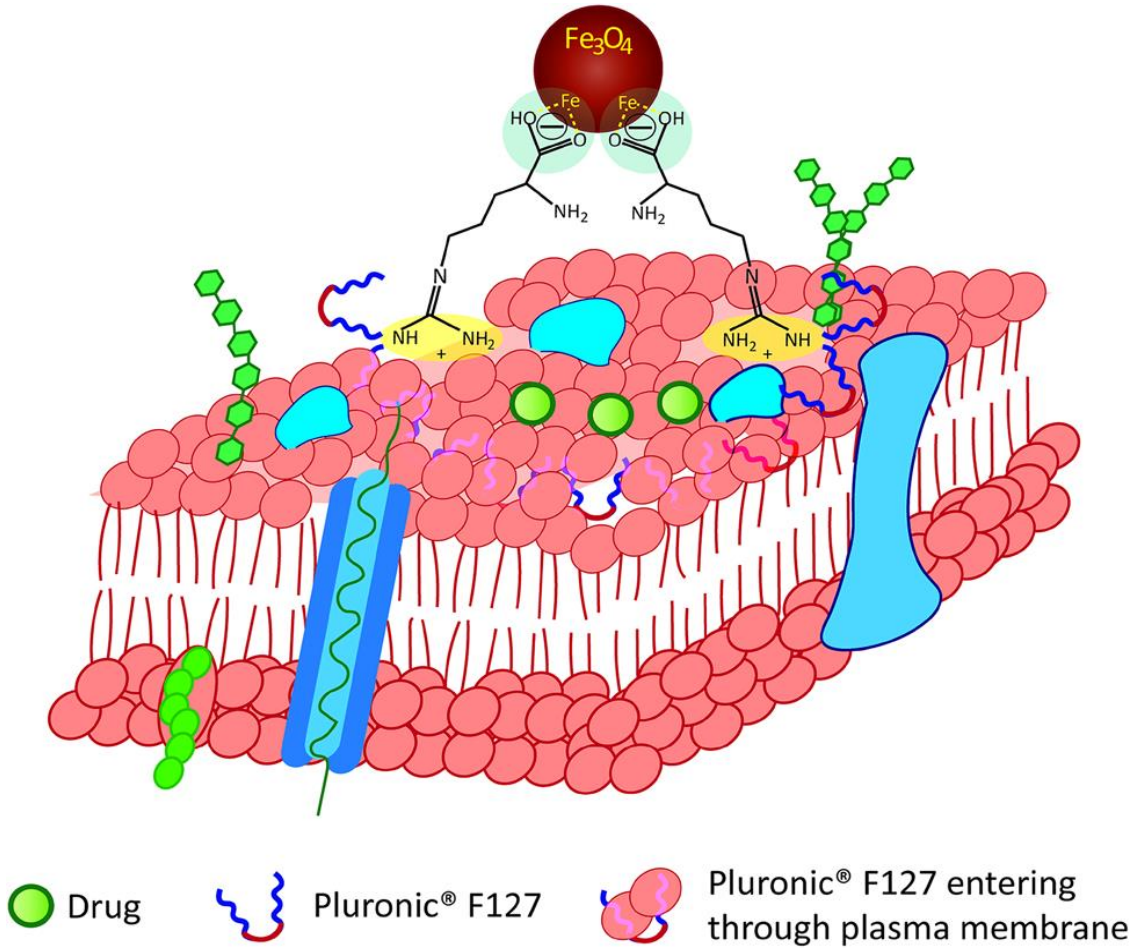

3.1 Introduction

Iron oxide-based materials find unique applications in modern science, particularly in the areas like drug delivery, cellular imaging, development of MRI contrast agents (CAs), hyperthermia induction, biosensing, and protein separation [1–3] Figure 3.1.

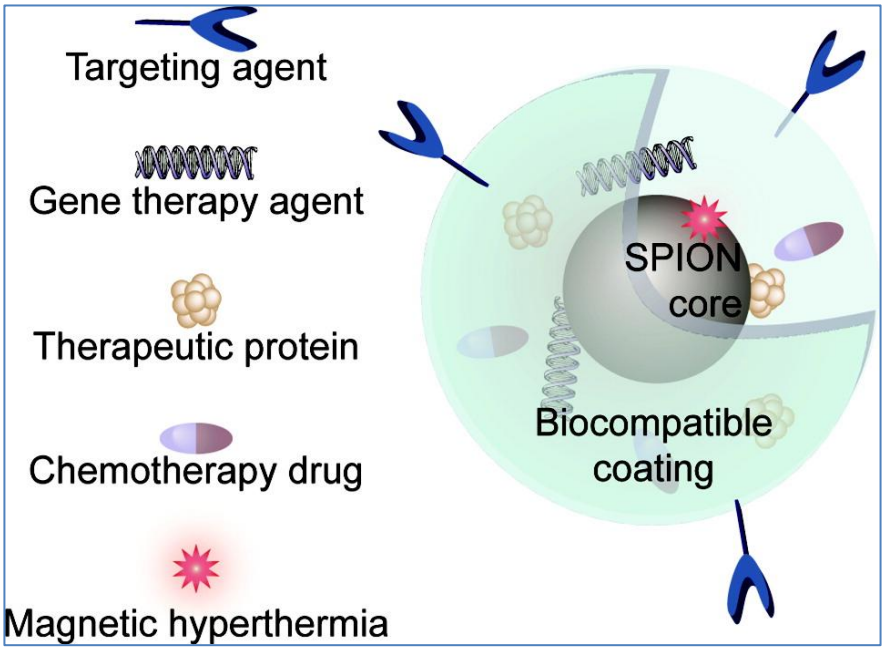

Fig. 3.1. Architecture of a nontherapeutic SPION [4].

The advantages of using magnetite for these applications are that it is non-toxic and decomposes into iron acting as an iron pool required for the synthesis of hemoglobin during erythropoiesis [5]. In bulk form, magnetite is paramagnetic having a large number of magnetic domains oriented randomly in absence of an applied magnetic field. On application of a magnetic field, they orient themselves in a single direction and revert to the random state on the removal of the field. However, it leaves some residual magnetization (ferromagnetic behavior) which is not desirable for applications like MRI contrast agents (CAs) or drug delivery platforms [6-7] (Figure 3.2).

It was observed that by decreasing the particle size to about 20 nm, these domains merged into a single domain having one collective magnetization direction on applying the field and, further, immediately got demagnetized on the removal of the field (superparamagnetic behavior) [8-9]. Any material having this property is perfect to serve as a drug delivery vehicle. However, by decreasing the particle size, magnetic material has a natural tendency to agglomerate [10-11] Figure 3.3. The ferro-fluid having a very less particle size in a given solvent system is unstable.

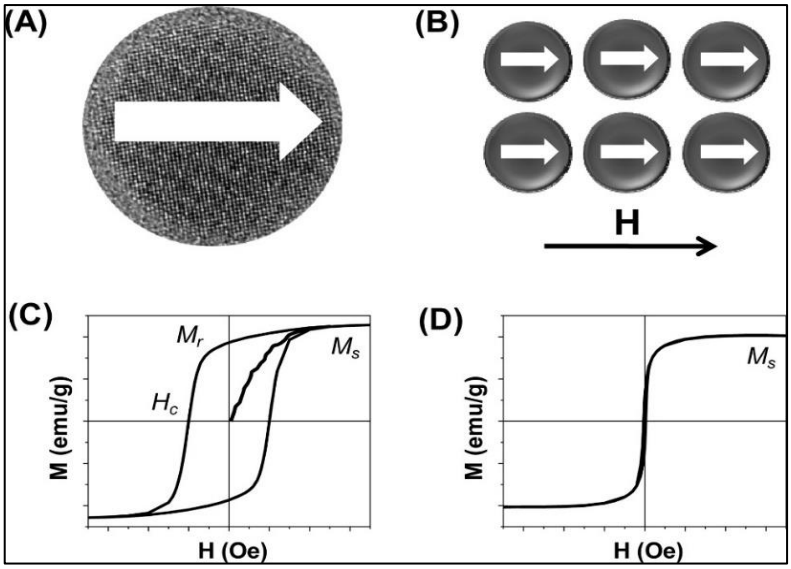

Fig. 3.2. (A) a single domain magnetic NP with its magnetization pointing to one direction, (B) a group of single domain magnetic NPs aligned along a magnetic field direction, (C) the hysteresis loop of a group of ferromagnetic NPs, and (D) the hysteresis loop of a group of superparamagnetic NPs. [12].

To make a stable suspension and prevent agglomeration, the surface of the particle is coated with molecules of surface active agents like CTAB, SDS, etc. However, such suspension shows toxicity at physiological pH. Hence, the surfactant-free synthesis of Fe_3O_4 nanoparticles (NPs) is desired [13-14].

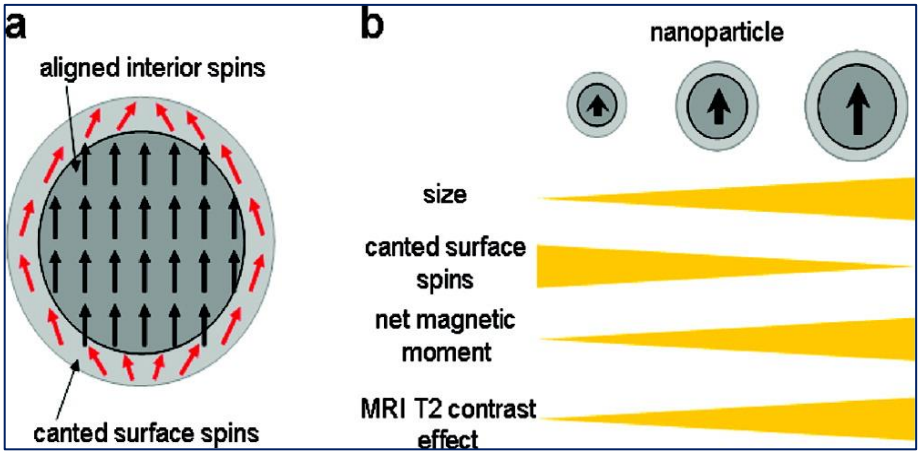

Fig. 3.3. Nanoparticle size effects on magnetism and MR contrast enhancement: (a) canted surface atoms surrounding core magnetic atoms; (b) surface to volume ratio vs size, canted surface spins, net magnetic moment, and T2 contrast effect [15].

3.1.1. *MR Imaging: The Concept*

MRI provides three-dimensional images by measuring proton relaxation processes of water molecules in a given system. Under an external magnetic field (B0), a small amount of the proton nuclei aligns in the direction of magnetic field, and the aligned nuclei start to precess gyroscopically with a net magnetic moment of m and a Larmor precession frequency of $\omega o = \gamma Bo$. A transversed resonant radio frequency (RF) pulse applied perpendicularly to B0 produces resonant excitation of magnetic moment precession into the perpendicular plane. After removing the RF, the magnetic moment eventually relaxes to equilibrium by realigning to B0. Two pathways are involved in such relaxation processes: longitudinal relaxation, which follows the loss of energy from the excited state to its surroundings (lattice), and transverse relaxation, which results from the loss of phase coherence of the precessing nucleus spins in the xy plane due to spin-spin interaction. (Figure 4a-c). These processes can be described using the following mathematical equations:

$mz = m(1 - e\text{-}t/T1)$ (longitudinal) ……(1)

and

$mxy = m \sin(\omega 0t + \varphi)e\text{-}t/T2$ (transverse)……(2)

where, T1 and T2 are the longitudinal and transverse relaxation time, respectively.

MRI captures such relaxation processes and reconstructs them to provide 3-D grayscale images. Areas with faster T1 relaxation are imaged with whiter contrast in T1-weighted MRI, whereas areas with faster T2 relaxation are imaged with darker contrast. Biological tissues and organs have aqueous environments with varying density and homogeneity, which are imaged as various contrasts and offer anatomical data. However, in other circumstances, the contrast between tissues (for example, normal vs malignancy) is too faint to offer precise imaging information. Furthermore, MRI only offers anatomical information, not molecular/biological information about the region of interest. Magnetic nanoparticle probes serve two functions: they improve contrast differences between biological targets and other tissues, and they also give molecular imaging capabilities. When exposed to a magnetic field of B0, nanoparticles exhibit a moment of magnetization. Additionally, an induced magnetic field creates a significant local perturbing dipolar field around the particle. Such local magnetic field in homogeneities reduce T2 and accelerate the dephasing rate of the Lamor precession of surrounding water molecules (Figure 3.4 d, e).

In the nanoscale regime, these values can be precisely tuned by controlling nanoparticle characteristics like size, shape, composition, and crystallinity. For example, smaller

nanoparticles with higher surface-to-volume ratios possess a weaker net magnetic moment due to the large contribution of canted magnetic spin states on the surface. The spin-spin relaxation time (T2) is inversely proportional to the square of the particle's magnetic moment (μ), according to eq 2.

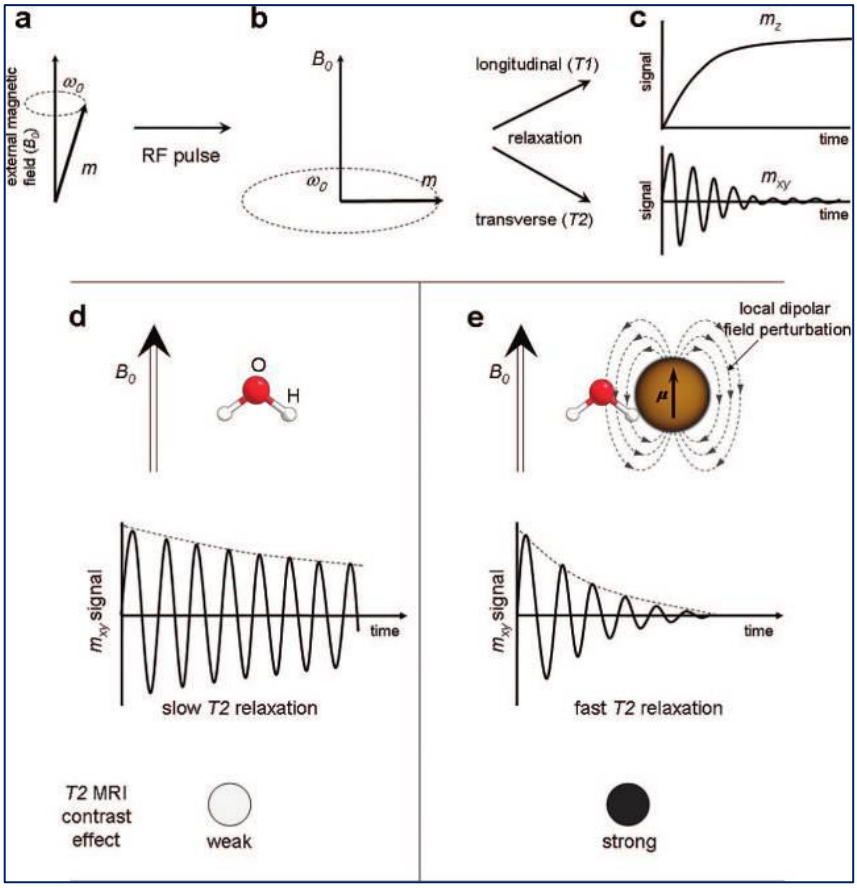

Fig. 3.4. Illustration of the magnetic resonance (MR) concept and the role of magnetic nanoparticles as a contrast agent: **(a)** Water protons' net magnetic spins (m) precess with a Larmor frequency (ω0); **(b)** RF pulses cause m to precess perpendicular to B0; **(c)** m relaxes back to its original equilibrium states through longitudinal (T1, mz) and transverse in-planar (T2, mxy) modes; **(d)** Without magnetic nanoparticles, water protons have a slow relaxation time with a weak MR contrast effect; **(e)** In the presence of magnetic nanoparticles, m relaxes faster [15].

Very few iron oxide-based MRI CAs are available in the market globally (e.g., Ferridex ®, Endorem®, and Resovist®) as compared to Gd-based CAs, even though there is an abundance of research reported in this area [16-17].

The main reasons are (i) magnetite NPs commonly act as *T*2 CAs (darkening the lesions) by

interrupting the signals coming from the lesions, and this requires more processing time compared to Gd-based *T*1 CAs (brightening the lesions), (ii) the dark lesions very often confused with other pathogenic situations like hemorrhages, fat deposits or calcification which necessitate supplementary pathological data to conclude the disease [18–20], (iii) their prolonged half-life in the body requires weeks to a month time to get cleared from the blood utilizing phagocytosis through macrophages (e.g. Kupffer cells) followed by uptake by the liver, spleen, and lymph nodes (Figure 3.5).

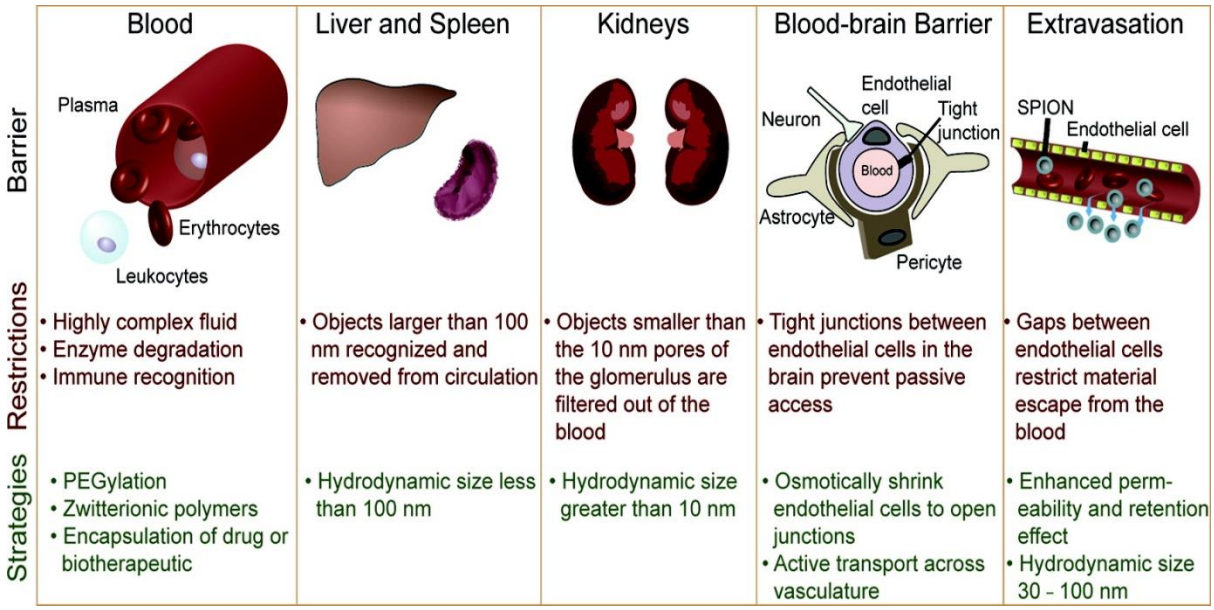

Fig. 3.5. Physiological barriers encountered by a typical therapeutic vehicle [21].

In contrast, Gd complexes get cleared from the body within minutes creating the contrast effect immediately post the entry into the target [22–24], (iv) their physical properties vary with particle size, and (v) the uniform particle size(monodispersity) of the suspension is crucial. It is achieved by adopting the synthesis route involving nonaqueous coordinating solvents (dodecane, oleylamine, etc.) at high temperature compels stringent experiment control [25], resulting in water-insoluble ferrofluid. A tedious procedure like ligand exchange through dialysis for more than 24 h is required to make the material hydrophilic and water soluble [26]. However, incomplete ligand exchange hampers the stability in aqueous media. Despite all these drawbacks, the attraction for the development of iron oxide-based theranostic agents remains intact. Affordable, non-toxic, and water-soluble magnetic theranostic agents can be developed by amending these process parameters [27]. The research

in this area gets momentum when it was observed that iron oxide NPs having less than 5 nm particle size show *T*1 contrasting ability (ES-MIONs) [28-29]. This is due to suppressed magnetization along a longitudinal axis which decreases *r*2 relaxivity and enhances r1 by diminishing the spin canting effect at a very small particle size (Figure 3.6). It is clear from this discussion that image contrasting ability can be adjusted by tuning the particle size of the Fe_3O_4 NPs. These can be achieved, in the case of Fe_3O_4, by fine-tuning the magnetic interactions among Fe^{2+}/ Fe^{3+} ions at crystal lattice sites. Bulk Fe_3O_4 NPs (80–100 nm) possess a high magnetic moment (80–120 emu/g) which distorts the background noise resulting in confused image contrasting [30]. Due to this, a very small cancerous lesion cannot be detected (e.g., early stage of cancer) or over-sighted [31]. These difficulties can be solved by modulating the magnetic moment of the NPs by doping with suitable ions.

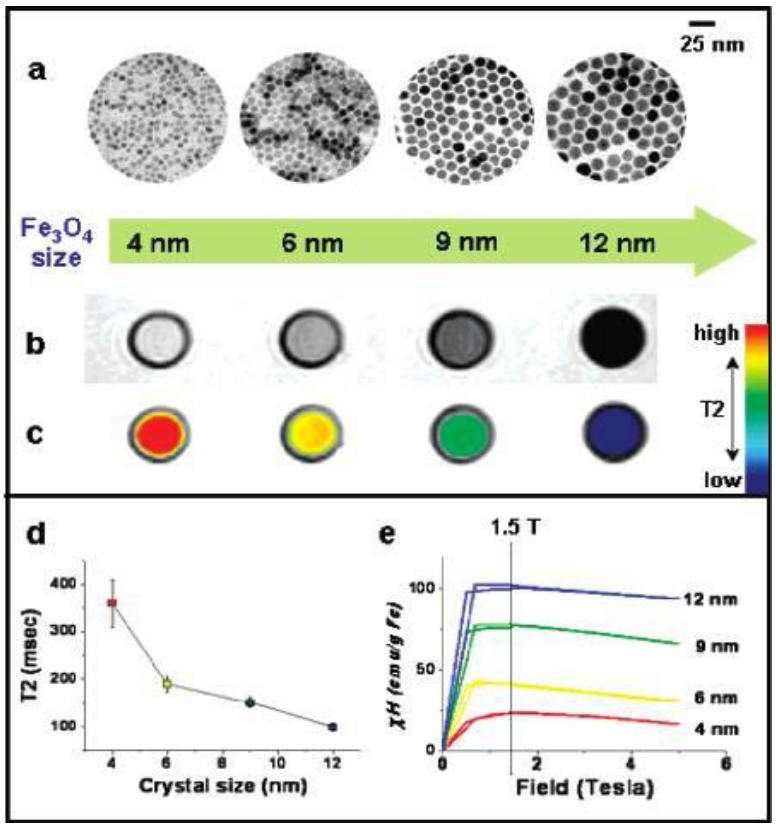

Fig. 3.6. (a) TEM pictures of Fe3O4 nanocrystals measuring 4 to 6, 9, and 12 nm. **(b)** Size-dependent T2-weighted MR images of Water-Soluble Iron Oxide (WSIO) Nanocrystals in aqueous solution at 1.5 T. **(c)** Color-coded MR images with T2 values show size-dependent variations from red to blue. **(d)** Graph comparing T2 value to WSIO nanocrystal size. **(e)** Magnetization of WSIO nanocrystals was measured using a SQUID magnetometer [32].

Brigatinib is a second-generation anaplastic lymphoma kinase (ALK) inhibitor known to be an effective pharmacological agent against numerous types of cancer. It is approved by the U.S. Food and Drug Administration for the treatment of non-small cell lung cancer (NSCLC) since April 2017 [33]. It acts to inhibit anaplastic lymphoma kinase (ALK), epidermal growth factor receptor (EGFR), and reactive oxygen species (ROS)—all of which are known drivers of NSCLCs [34]. It has been documented that ALK, ROS, and EGFR can induce a series of phosphorylation reactions responsible for the up-regulation of the oncogenes like NPM and EML4 [35]. Brigatinib is reported to block phosphorylation and prevents the progression of the cell cycle in cancerous cells [36]. The side-effects like diarrhea, nausea, abdominal pain, constipation, dizziness, fever, headache, trouble sleeping, joint pain, lowering of blood pressure, etc., due to high (or initial) dosage of brigatinib can be overcome when targeted delivery to the cancerous lesion carried out.

In light of these, the anti-cancer activity of brigatinib was evaluated in vitro on a representative model of NSCLC epidermoid carcinoma cell line A431 on loading with various as-synthesized magnetite-based drug delivery vehicles.

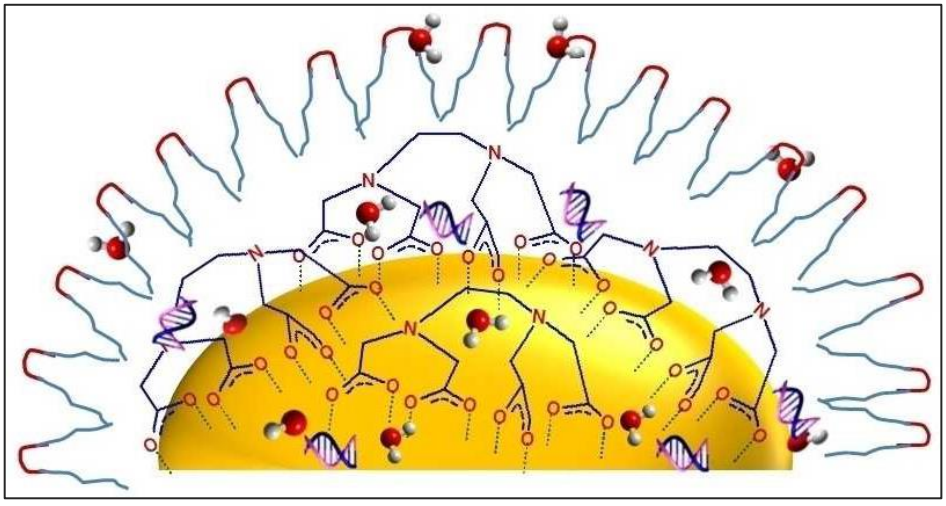

Fig. 3.7. Our previous study, Cartoon showing a Fe_3O_4/edta/P magnetic gene delivery vehicle. Central hemisphere represents Fe_3O_4 nanoparticle surrounded by edta ligands (coordinate with surface Fe ions). The outer zigzag light blue lines correspond to hydrophobic PPO blocks while that of red to hydrophilic PEO blocks. Some water molecules can be seen entrapped near the ligand's nitrogen atoms by coordination bond while the polymeric micelle is surrounded by second sphere water molecules. Plasmid can be seen entrapped near inner surface water molecules and hydroxide ions [37].

In previous studies, we demonstrated that Fe_3O_4 NPs having the surface modified by suitable small amino acid molecule (L-proline) and enveloped by amphiphilic block copolymers such as Pluronic F-127 can be used as a vehicle to conjugate drug/gene (Figure 3.7 & 3.8) [37-38].

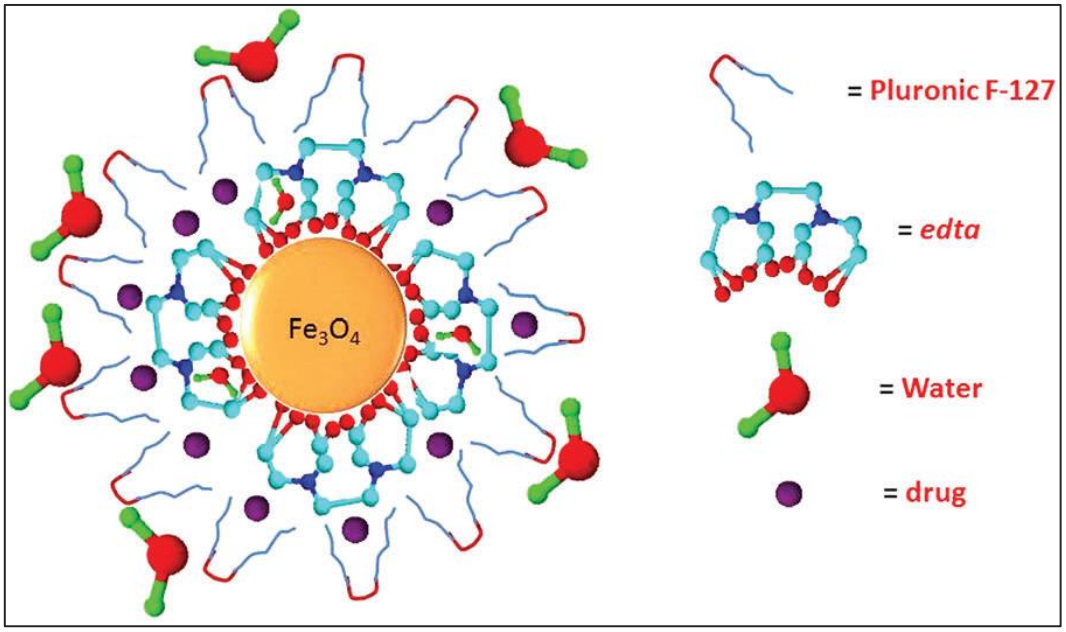

Fig. 3.8. Our previous work. Cartoon showing a Fe_3O_4/EDTA/P magnetic polymeric micelle. Central orange ball represents an Fe_3O_4 nanoparticle surrounded by EDTA ligands (blue balls indicate nitrogen, light blue for carbon, red for carboxylate groups, purple for drug molecules). The zigzag light blue lines correspond to hydrophobic PPO blocks while that of red to hydrophilic PEO blocks. Some water molecules can be seen entrapped near the ligand's nitrogen atoms by coordination bond while the polymeric micelle is surrounded by second sphere water molecules [38].

It is well established that such kind of platforms can effectively load and deliver the cargo to the target and also function as MRI CAs. Moreover, most of the syntheses reported to date are carried out in constrained conditions to stringently control the particle size and phase purity of the magnetite. However, during large-scale production, such conditions may not be strictly followed as some minute errors during unit operations could result in wastage of the total batch and make it economically unviable. In this study, we have synthesized Ultra-Small Iron Oxide NPs (Fe_3O_4-USIONs) and ferrites (MFe_2O_4) by a simple co-precipitation method and these L-arginine-modified and Pluronic F127 ®-coated Fe_3O_4 NPs (Fe_3O_4@L Arg/P) evaluated as drug delivery platform and MRI CAs. We focused on tuning the intrinsic magnetic property of USIONs by varying the transition metal dopant ions under the same

reaction conditions rather than adopting the solvothermal or any other tedious synthesis methods. We report, here, the tuning of magnetism and improvement as well as the reversal of contrasting ability by doping Fe_3O_4 with suitable transition metal ions (Zn^{2+}, Mn^{2+}, and Ni^{2+}).

We have demonstrated by in vitro studies that doped magnetite shows higher drug delivery efficiency with improved performance as MRI CAs. It has been demonstrated that the parameters (like τM, τR, q, etc.) proposed in Solomon-Bloembergen-Morgan (SBM) theory for paramagnetic relaxation can also be applicable in the case of Fe_3O_4-based NPs system in terms of hydrogen bonding to modulate the $T1$ contrasting in MRI.

3.2 Experimental

3.2.1 Materials

Ferric chloride $FeCl_3.6H_2O$, $ZnCl_2$, and $MnSO_4$ were obtained from Loba Chemicals, India. Ferrous chloride $FeCl_2.2H_2O$ and an aqueous solution of ammonia were purchased from S.D Fine Chemicals, India. Pluronic® F-127 and L-arginine were purchased from Sigma-Aldrich. All chemicals were of AR grade and used without further purification.

3.2.2 Synthesis of brigatinib-loaded Fe_3O_4@L-Arg/P magnetic micelles (Fe_3O_4@L-Arg/P/bg):

In total, 300 mg of Fe_3O_4 NPs was dispersed in 30 mL of DI water and then 100 mg of Pluronic® F-127 was added. The mixture was then stirred overnight on a magnetic stirrer at RT and then centrifuged at 6000 rpm for 5 min to form Fe_3O_4@L-Arg/P NPs. In total, 30 mg of these NPs was dispersed in 10 mL of DI water. To it, 2 mL of the drug solution (4.5 mg mL^{-1}) was added and the mixture was stirred vigorously at RT for 24 h. The drug-loaded Fe_3O_4 NPs were allowed to settle down by a magnet. The drug-loaded NPs were suspended in DI water and washed twice (Scheme 1). The same procedure was adopted for Zn^{2+}, Mn^{2+}, and Ni^{2+}- doped Fe_3O_4 NPs.

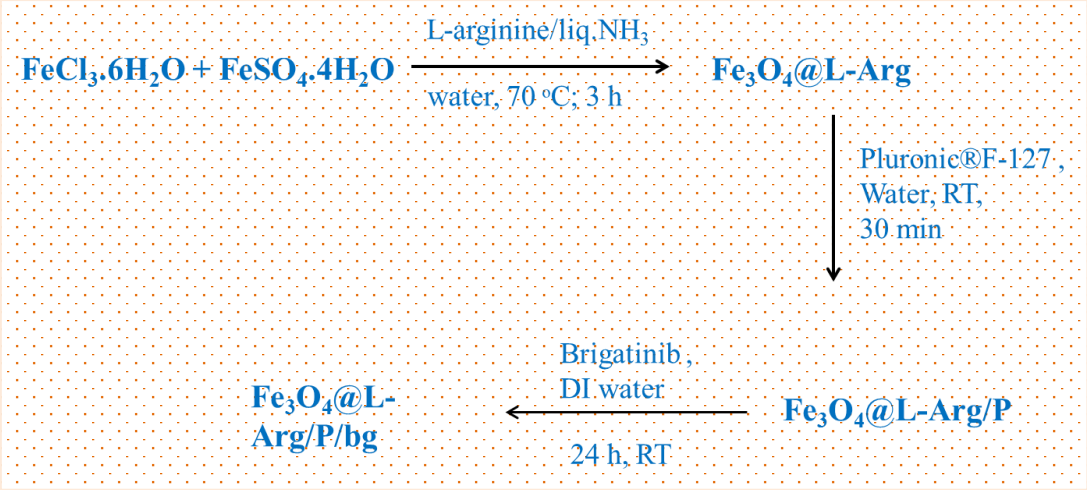

Scheme 3.1. An overall synthesis scheme of developed drug delivery vehicle and MRI contrast agents

3.3 Result and Discussion

3.3.1 Phantom study

The efficiency of the CAs depends upon their ability to shorten the relaxation time of the protons in the vicinity. Under the influence of an applied magnetic field, the excited protons having spins parallel to the field resonantly absorb the electromagnetic energy irradiated by radio waves. This results in the spins being anti-parallel to the field. These high-energy spins relax back to the original state on the removal of the radio waves through two relaxation processes: (i) longitudinal relaxation indicated by relaxation time T1 required to recover 63% magnetization of the equilibrium value and (ii) transverse relaxation expressed by time T2 required to drop the 37% magnetization of its initial magnitude. These relaxation processes directly affect the MRI signal intensity and as per definition, T1 enhances the signal intensity while T2 diminishes the same, and CA present in the vicinity of the protons perturb these processes referred to as positive or negative contrast agents, respectively. Hence, positive CAs shorten the T1 which makes the signal recovery fast which in turn enhances the signal intensity producing a bright image. Negative CAs shorten the T2 of the protons by dropping the transverse magnetization quickly resulting in a loss of signal intensity and creating a dark image [6, 39] (Figure 3.9).

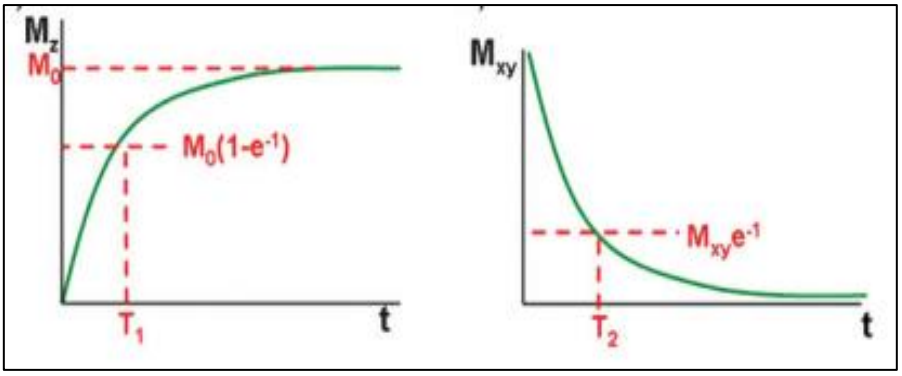

Fig. 3.9. T1 relaxation and T2 relaxation in MR processes [6, 39].

The efficiency with which the CA enhances the proton relaxation rate of water is referred to as relaxivity (r). The r_1/r_2 ratio is used as a marker to decide whether the CAs work as a positive or a negative. Good T1 CAs have r_2/r_1 less than 5 and T2 CAs have a high r_2/r_1 ratio (>10) [5]. The correlation between T1 or T2 relaxation rates (R_1 or R_2) and the concentration of CAs can be investigated through the phantom study Figure 3.10.

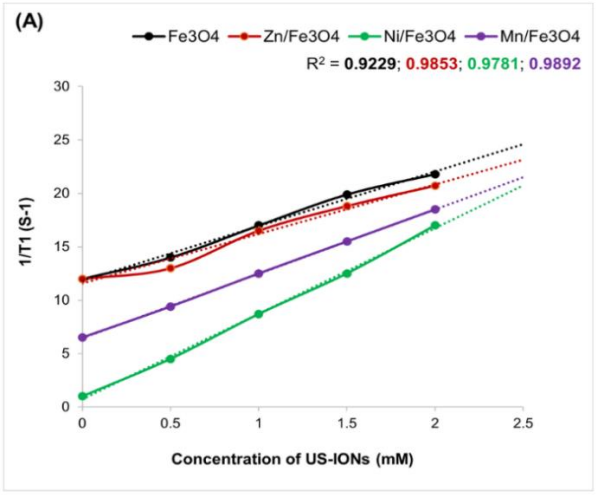

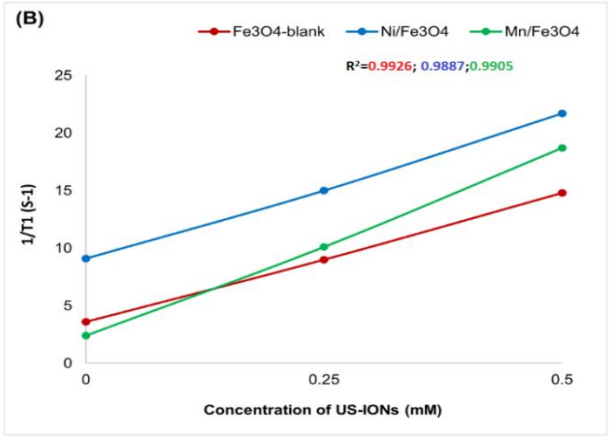

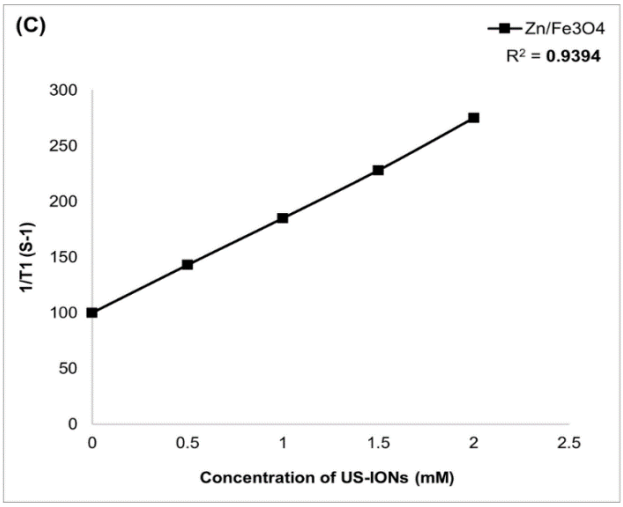

Fig. 3.10. A 1/*T*1 **B** and **C** 1/*T*2 Vs concentration of M^{2+}/ Fe_3O_4@L-Arg/P NPs

It can be observed from Figure 3.10 that the relaxation rates vary linearly with the concentration of NPs. The longitudinal relaxivity (r_1) or transverse relaxivity (r_2) were calculated from the slope of the lines and are reported in Table 1.

Table 1. Longitudinal and transverse relaxivities and their ratio of as-synthesized M^{2+}/ Fe_3O_4@L-Arg/P NPs.

Sample	r_2 ($mM^{-1}s^{-1}$)	r_1 ($mM^{-1}s^{-1}$)	r_2/r_1
Fe_3O_4@L-Arg/P	21.49	5.27	4.079
Zn^{2+}/Fe_3O_4@L-Arg/P	86.57	4.52	19.17
Ni^{2+}/Fe_3O_4@L-Arg/P	24.36	7.70	3.16
Mn^{2+}/Fe_3O_4@L-Arg/P	32.40	6.05	5.35

It can be observed that blank Fe_3O_4@L-Arg NPs can generate bright contrast, contrary to their inherent nature of producing a dark image. This is due to the very small particle size as explained earlier. On Zn^{2+} doping, there is a small decrease in r_1 values compared to blank Fe_3O_4 while that of r_2 increases drastically increasing the r_2/r_1 ratio, which qualifies the material to act as a T2 CA. It can be observed from Table 1 that blank Fe_3O_4@L-Arg/P NPs

show 5.27 $mM^{-1}s^{-1}$ r_1 relaxivity while the commercial Gd-DTPA complex has an r_1 value of ca. 4 $mM^{-1}s^{-1}$ and that of Ferridex® has ca. 10 $mM^{-1}s^{-1}$ (used as T2 CAs due to its very high r_2 value). Hyeon group studied T1 contrast enhancement in extremely small iron oxide NPs (ESIONs) having 2.2, 3, and 12 nm diameter and the observed r_1 values 4.78, 4.77, and 2.37 $mM^{-1}s^{-1}$ respectively [24]. In the present case, Zn^{2+}/Fe_3O_4@L-Arg/P NPs show almost a similar value (4.52 $mM^{-1}s^{-1}$) while blank, Ni^{2+} and Mn^{2+} doped Fe_3O_4@L-Arg/P show a gradual increase in r_1 up to 7.70 $mM^{-1}s^{-1}$. These results indicate that H-bonded inner sphere water molecules can increase the r_1 relaxivity up to ca. 3-4 $mM^{-1}s^{-1}$.

On doping Zn^{2+}ions, the Ms value drastically increased resulting in a superparamagnetic material. This effect is due to replacing Fe^{3+} ions present at the Td sites in an inverted spinel structure. As a consequence, there is a decrease in antiferromagnetic communication among the Fe^{3+} ions at the Td and Oh sites which cannot cancel out the spin completely, resulting in the enhancement of Ms [40]. On doping with Mn^{2+}, the r_2 relaxivity increases from 21.5 to 32.4, however, that of r_1 also increases from 5.37 to 6.05 producing a low r_2/r_1 ratio enabling the material to act as T1 CA. The M-H plot also corroborates this result showing paramagnetic behavior with very small particle size. It has been observed that Mn^{2+} has a preference for both Td and Oh sites resulting in a mixed spinel structure. In the present case, it is confirmed from the Mössbauer spectroscopy that Mn^{2+} ions substitute Fe^{2+} from Oh sites, feeding the unpaired electrons in the sites which results in enhanced communication among the electronic spins resulting in a rise in r_2 relaxivity. This substitution of ions also synergistically reduces the proton relaxation time to recover the longitudinal magnetization thereby increasing the r_1 [41]. On doping with Ni^{2+} replaces Fe^{3+} and Fe^{2+}/Fe^{3+} from Td and Oh sites facilitate the electronic spins to couple ferromagnetically and enhance the Ms. However, in the present case, both r_1 and r_2 relaxivities increases giving rise to low relaxivity ratio. Hence, doping with Ni^{2+} in USION synergistically enhances the recovery of longitudinal magnetization and enables the material to act as a T1 CA.

3.3.2 MRI Study

The sequences of the radio frequency signal repetition time (TR) and the detection or echo time (TE) were designed such that the T1-weighted and T2-weighted images of the cross-section of a capillary containing the sample in a coronal mode can be captured in an MRI machine [42].

Table 2. T2 weighted (TR = 3000/TE = 98.8 ms) MR images for different concentrations M^{2+}/Fe_3O_4@L-Arg/P NPs systems.

Sr. No.	Sample	Concentration (mM)					
		0.5	0.25	0.1	0.05	0.01	0.001
1	Fe_3O_4@L-arg/P						
2	Zn^{2+}/Fe_3O_4@L-arg/P						
3	Ni^{2+}/Fe_3O_4@L-arg/P						
4	Mn^{2+}/Fe_3O_4@L-arg/P						

Table 3. T1 weighted (TR = 800/TE = 11.5 ms) MR images for different concentrations of M^{2+}/Fe_3O_4@L-Arg/P NPs.

Sr. No	Sample	Concentration (mM)					
		0.5	0.25	0.1	0.05	0.01	0.001
1	Fe_3O_4@L-Arg/P						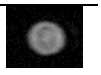
2	Zn^{2+}/Fe_3O_4@L-Arg/P						
3	Ni^{2+}/Fe_3O_4@L-Arg/P						
4	Mn^{2+}/Fe_3O_4@L-Arg/P						

It can be observed from Tables 2 and 3 that blank Fe_3O_4@L-Arg/P NPs produce bright images at very low concentrations (0.001 mM) and doping Ni^{2+} synergistically brightens the image at this low concentration. This effect is continued up to 0.1 mM. Then the image gets distorted at higher concentrations (0.25 and 0.5 mM). In the case of Zn^{2+}/ Fe_3O_4@L-Arg/P NPs, the T2 contrasting effect is achieved at 0.1 mM while higher concentrations (0.25 and 0.5 mM) are not effective in producing a dark image. No contrasting effect was produced in the case of Mn^{2+}/Fe_3O_4@L-Arg/P at a low concentration range. This material produces a T1 contrast effect at 0.5 mM.

3.4 Discussion

The commercially available Gd-DTPA and Gd-DOTA complexes have their ninth valence satisfied by a water molecule (q = 1) (Figure 3.11).

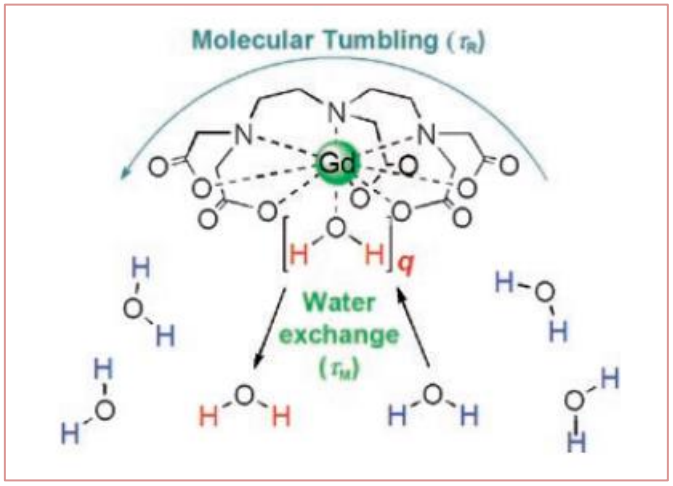

Fig. 3.11. Key parameters affecting the proton relaxivity r [43].

There is a very small energy difference between their eighth and ninth valence. Hence, the ninth coordinated water ligand is labile and continuously gets exchanged with bulk water molecules [43].

This process is dynamic. Due to this, the molecular tumbling increases. These commercial CAs have one coordinated water molecule (q=1), however, the complexes with q = 2, 3, and 4 have also been developed to increase the r1 relaxivity of bulk water protons in an applied field which in turn, enhances the T1 contrasting. The efficiency of T1 CAs depends on three parameters (eq.1)

$$\left(\frac{1}{T_1}\right) = q.\ P_m \left[1/(T_{1m} + \tau_M)\right] \quad \text{——— (1)}$$

Where T_{1m} is the longitudinal relaxation time of the inner-sphere bounded water protons, q is the number of coordinated water molecules in the first coordination sphere, P_m is the mole fraction of water coordinated to the metal center (in the case of Gd complexes) and τ_M is the mean water residence time near the metal center. If the value of τ_M is very small then it results in only ($1/T_{1m}$), the relaxation rate of inner-sphere water. Hence, a high relaxation rate depends on a higher value of q. The SBM theory for paramagnetic relaxation suggests that optimization of correlation time (τ_c) is essential to obtain higher relaxivity (eq. 2) [44].

$$\left(\frac{1}{\tau_{ci}}\right) = \left(\frac{1}{\tau_M}\right) + \left(\frac{1}{\tau_R}\right) + \left(\frac{1}{T_{ie}}\right) \qquad i = 1,2 \text{ \_\_\_\_\_} (2)$$

The Gd-DTPA chemistry for proton relaxivity to produce bright MR images is well established and predicted by SBM theory [42, 45]. However, to avoid the problems concerning free Gd leaching and consequent complications due to toxicity, the development and application of iron oxide-based MRI CAs having the capability to induce longitudinal relaxation of water protons (for brighter images) need focused attention. The H-bonding can arrange the water molecules in a definite order and its strength can be modulated by varying the donor hetero atoms and acceptor H atoms present in the ligand. These molecules can in turn be compacted by an outer polymeric surfactant micelle. This strategy can control the molecular tumbling (τ_R) of the water molecules. From a three-dimensional perspective, there can also be a faster water exchange between these surface-ligand-bound H-bonded water molecules and those of the bulk water molecules through diffusion.

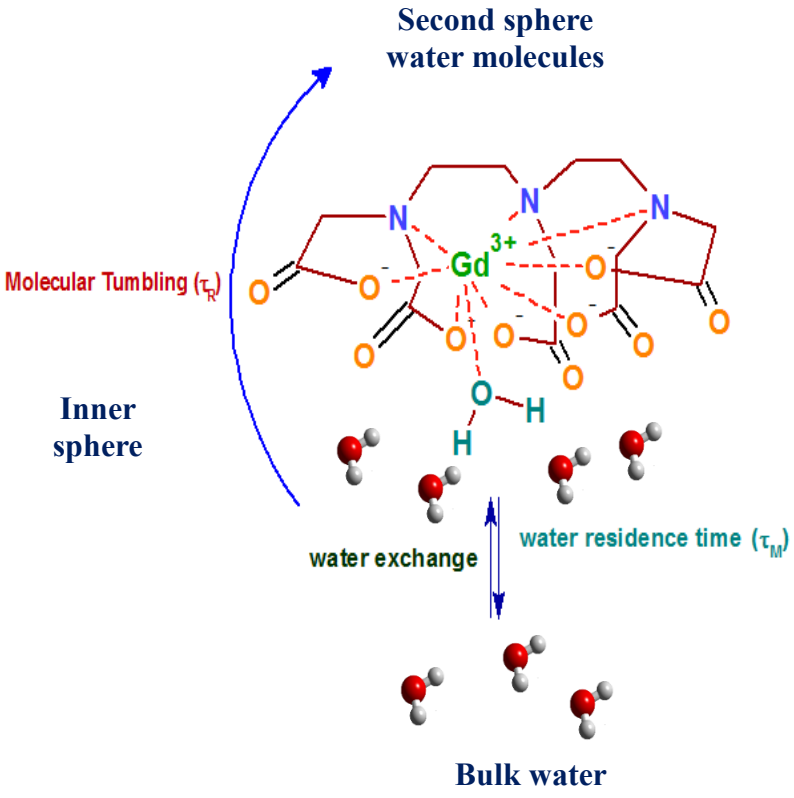

Gd-DTPA T1 Contrast agent: well-established chemistry. Proton relaxivity can be predicted by SBM theory [58].

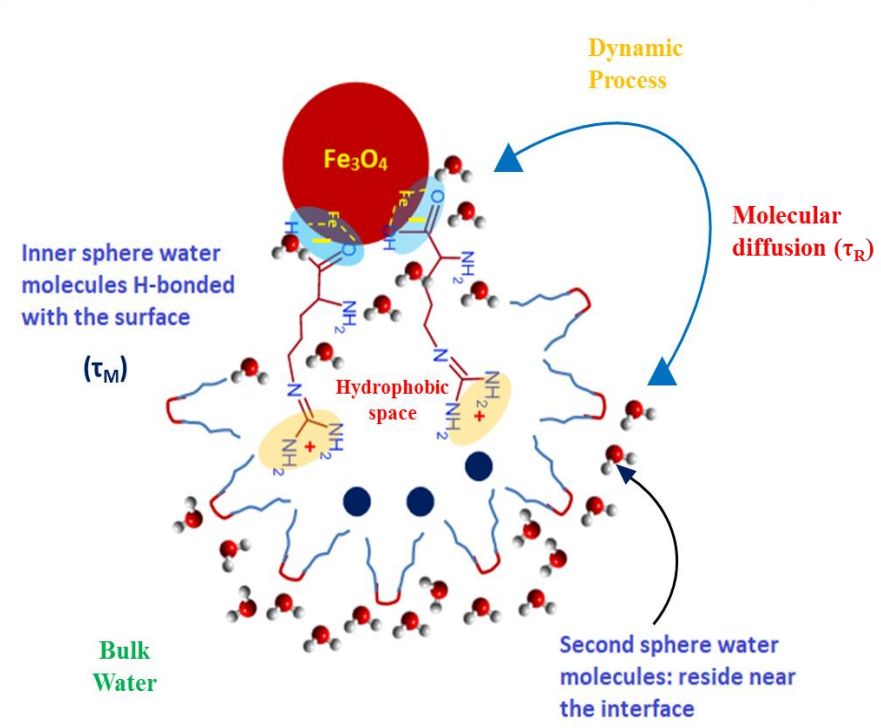

Scheme 3.2. The upper panel shows standard Gd-DTPA chemistry from SBM theory. The lower panel shows the proposed Gd-DTPA mimic based on the proposed tuning of the core@shell environment of USIONs.

In this way, the τ_M parameter can be controlled. The advantage of this strategy is that the number of inner spheres water molecules (q) will be more than one and this high number will collectively make the electronic relaxation time (T_{ie}) longer. Overall, high proton relaxivity can be achieved by tuning both the core as well as the shell environment in the developed USIONs (Scheme 3.2).

3.5 In vitro drug release kinetics, cell-viability, and cytotoxicity studies

The M^{2+}/Fe_3O_4@L-Arg/P NPs were tested as drug delivery vehicles for the epidermoid carcinoma cell line A431 to evaluate the anti-cancer activity of the loaded drug (Brigatinib). The smooth release, cytotoxicity, and colony-forming ability of these formulations were checked by the drug release kinetics, MTT, and clonogenic assays respectively. A wide range of doses as described in the individual experiments were used to make a comparison among the formulations (M^{2+}/Fe_3O_4@L-Arg/P/bg).

3.5.1 In v*itro* drug release kinetic study

The kinetics of *in vitro* release of brigatinib from M^{2+}/Fe_3O_4@L-Arg/P (Figure 3.12) was studied in PBS solution at 7.4 pH (Figure 3.2). It can be observed that Mn^{2+}/Fe_3O_4@L-Arg/P/bg USIONs showed fast initial release as compared to those of Ni^{2+} doped. Mn^{2+}/Fe_3O_4@L-Arg/P/bg USIONs release 30% of the drug in a first burst in 5 h and the next 20% release in 72 h with an overall 50% release in three days. Approximately 70% drug was released from Ni^{2+}/Fe_3O_4@L-Arg/P/bg in three days. The Mn^{2+}/Fe_3O_4@L-Arg/P/bg USIONs started to release the drug early, however, took a long time to reach the 70% release rate than Zn^{2+} and Ni^{2+} doped vehicles. From this release kinetics study, it can be said that the release efficiency of the delivery vehicle is modulated by varying the dopant ions.

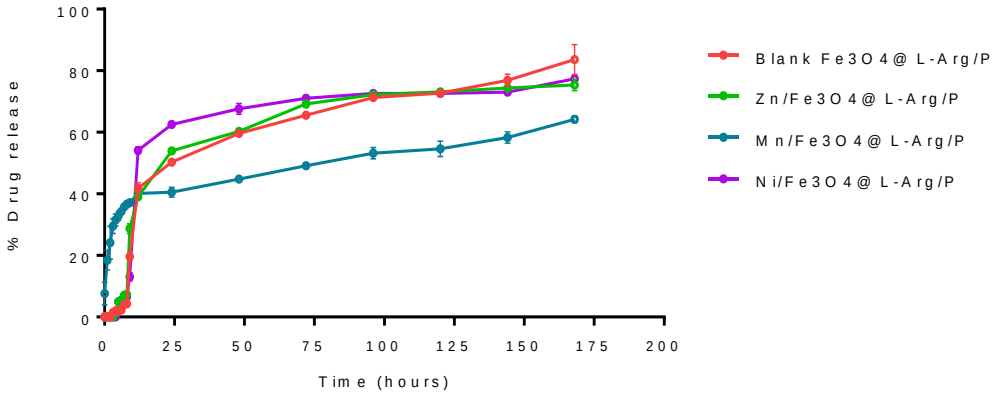

Fig. 3.12. Percentage release of Brigatinib from blank, Zn^{2+}, Mn^{2+}, and Ni^{2+} doped Fe_3O_4@L-Arg/P/bg. The drug released from Mn^{2+} doped Fe_3O_4@L-Arg/P/bg is the earliest as compared to others. However, at the end of three days (72 hours), more drug is released from Zn^{2+} and Ni^{2+} doped USIONs than Mn^{2+} doped ones.

This might be due to the restructuring of the surface. The defect produced due to the mismatch of the atomic radius of the dopant and host responsible for the physical interaction of the surface with the ligand and the drug molecules, in turn, affects the smooth release of the drug.

3.5.2 Cytotoxicity Study

The cytotoxic effect of the synthesized USIONs with or without the drug was studied by MTT assay, on the A431 human epidermoid carcinoma cell line (Figure 3.13). The bare drug remains inactive towards cell viability at microgram level dosage. However, the drug-loaded USIONs (M^{2+}/Fe_3O_4@L-Arg/P) affect it at the same level of dosage. M^{2+}/Fe_3O_4@L-Arg/P/bg USIONs with 10 µg/mL dose can reduce the cell viability to 53, 31, and 94 for Zn^{2+}, Mn^{2+},

and Ni^{2+}, respectively. In the case of the blank carrier (Fe_3O_4@L-Arg/P), the % cell viability remains basal even at higher dosages emphasizing the safety of the developed delivery platforms. Mn^{2+}/Fe_3O_4@L-Arg/P/bg boost the significant cell death at very low dosage levels as compared to Zn^{2+}/Fe_3O_4@L-Arg/P/bg system (Figure 3.13B and D) while Ni^{2+}/Fe_3O_4@L-Arg/P/bg NPs induce the cell death at very high concentration (1000 µg/mL) and does not reduce the cell numbers even if it can release the drug easily (Figure 3.13).

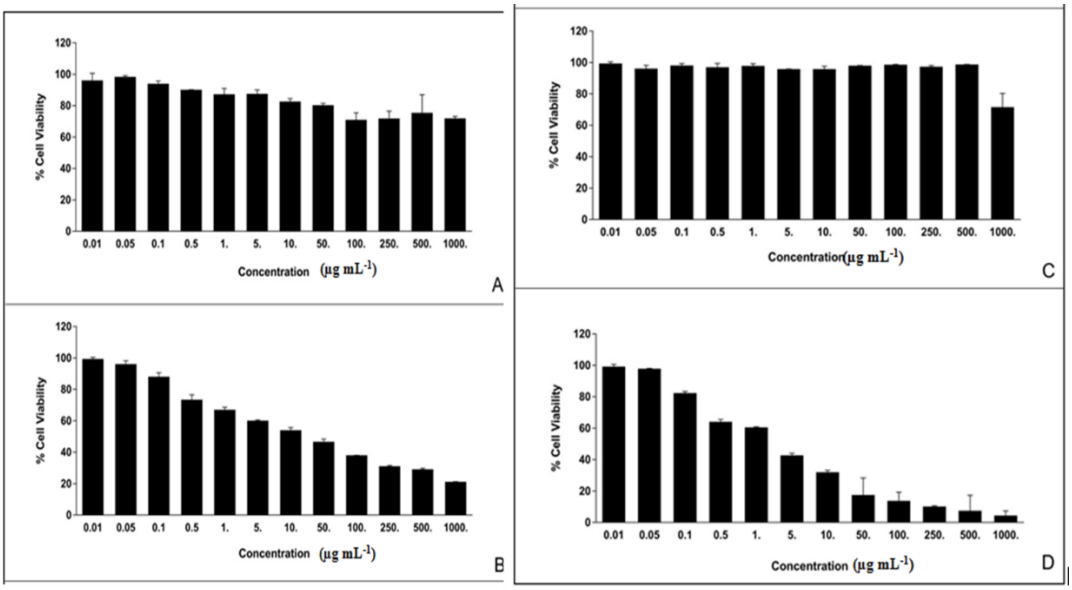

Fig. 3.13. Cell viability study.

A: Cells added with brigatinib only showed a reduction in viability after the concentration of drug was increased to 100 µg mL^{-1}. Cell mortality was observed to decrease the least even at 1000 µg mL^{-1} dosage of the drug;

B: Cell viability decreased even at a concentration as low as 1 µg mL^{-1}in case of Zn^{2+}/ Fe_3O_4@L-Arg/P/bg. Almost all the cells died at 1000 µg mL^{-1};

C: Cell death alleviated only at 1000 µg mL^{-1} concentration of this formulation. The hike in cell death was not as sharp as observed in the case of Mn and Zn doped Fe_3O_4@L-Arg/P/bg. Ni^{2+} doping, in fact, showed less cell death than that of the bare drug.

D: Only 0.1 µg mL^{-1}concentration of Mn^{2+}/ Fe_3O_4@L-Arg/P/bg could reduce cell viability. The rate of cell death increased rapidly after a concentration of 10 µg mL^{-1}. Which led to a complete culture death at about 1000 µg mL^{-1}.

3.5.3 Clonogenic Assay

The *in vitro* cell survival assay is based on the ability of a single cell to grow into a colony. It is generally carried out to determine the effect of a drug on the proliferation of tumor cells. The MTT assay demonstrated the high efficiency of the formulations as compared to the bare drug. It sheds light on the ability of the formulations to prevent colony formation often exhibited by cancer tumor cells.

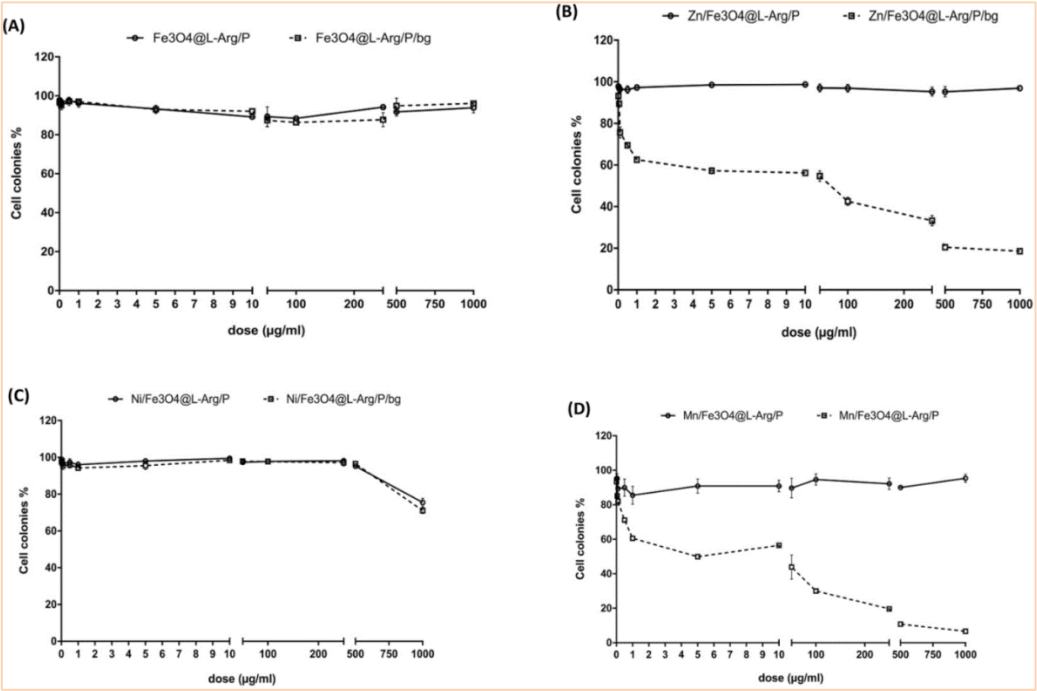

Fig. 3.14. Clonogenic assay

(**A**) No visible change in the plates was observed in presence of the bared drug at any concentration (in µg level). The number of colonies remained constant throughout.

(**B**) colony formation was reduced early at 1 µg mL^{-1} of the Zn^{2+}/Fe_3O_4@L-Arg/P/bg. Only a handful of colonies were observed at 500 to 1000 µg mL^{-1} of formulation.

(**C**) No change in the number of colonies on the addition of Ni^{2+}/Fe_3O_4@L-Arg/P/bg. The reduction in the number of colonies observed above 500 µg mL^{-1} dose.

(**D**) The colony formation drastically decreased at 1 µg mL^{-1} dose of Mn^{2+}/ Fe_3O_4@L-Arg/P/bg formulation. The number of colonies continues to decrease due to an increase in cell death.

It can be observed from Figure 3.14 B and 3.14 D that only 50% of colonies survived in the case of Zn^{2+}/Fe_3O_4@L-Arg/P/bg and Mn^{2+}/Fe_3O_4@L-Arg/P/bg at about 50 µg/mL dosage, while Ni^{2+}/Fe_3O_4@L-arg/P/bg did not cause any reduction in colony number at that concentration (Figure 3.14). These results indicate that Ni^{2+}/Fe_3O_4@L-Arg/P/bg can act as

good delivery vehicle as compared to the other developed vehicles.

Hence, the present study emphasizes that the efficiency of the vehicle to release the drug is its integral property and is influenced by the factors like the surface-ligand binding strength, the surrounding environment of the entrapped drug molecules, the perturbance of the core's magnetism by dopant ions, etc. It would be interesting to carry out *in vivo* studies regarding drug delivery and MR imaging, which will be the focus of our next study.

3.6 Conclusion

Small amino acid molecules like L-arginine can act as capping and chelating ligands to bind Fe_3O_4 nanoparticles tightly, restrict their growth at the nanoregime, and form USIONs. Pluronic F127 encapsulates L-Arg capped USIONs effectively and forms polymeric micelles while retaining magnetic properties. The synthesized Pluronic encapsulated and L-Arg capped Fe_3O_4 magnetic micelles can act as drug delivery platforms to load the hydrophobic anti-cancer drug Brigatinib in their hydrophobic shells. Blank, Mn^{2+}, and Ni^{2+} doped Fe_3O_4@L-Arg NPs reveal T1 contrasting ability while those of Zn^{2+} doped NPs show T2 contrasting due to the modification in relaxivity ratio. Out of these, Ni^{2+} doped USIONs are the best T1 CAs. The drug-loaded Ni^{2+}/Fe_3O_4@L-Arg/P/bg exhibits good drug release kinetics. But the MTT assay suggests the need for a higher dosage to produce a pronounced effect. In this context, Mn^{2+} doped vehicles are more efficient. Only a very low dosage is required for cell death and it is also true for colonogenic assay. *In vitro* cellular uptake of drug-loaded magnetic micelles by epidermoid carcinoma cell line (A431) shows more internalization than the bare drug. The overall size of the drug-loaded magnetic micelles allowed prolonged circulation and sustained drug delivery. Toxicity studies confirm the safety of the developed iron oxide nanoparticle-based magnetic micelles as drug delivery vehicles at a dosage range of 0.125–0.25 mg/mL. Rationally, it can be claimed that Mn^{2+} doped USIONs are very suitable for theranostics applications. This study leaves some questions unanswered like (1) how do dopant ions and consequent modification in the magnetic property of the core (by maintaining the shell environment constant) affect the drug release kinetics and proliferation of tumor cells? (2) Can the strength of the H-bonds among surface-bound ligands and water molecules in the shell environment be evaluated to study the proton relaxivity of bulk water? (3) Can the contrasting ability of the MRI CAs be modulated by varying only the shell environment and keeping the core/core size constant? Further research is required to answer these questions.

3.7 Characterization

3.7.1 Calculation of drug loaded nanoparticles:

The amount of drug-loaded nanoparticles was calculated by using UV-visible spectroscopy. A drug solution in the concentration range from 0.5 to 9.0 mg mL^{-1} was prepared to construct a calibration curve. It was found that for every 1 mg of NPs, 0.096 mg of the drug was loaded out of 0.150 mg of the bare drug.

$$\left(\frac{1}{T_1}\right) = q.\ P_m \left[{}^{1}/_{(T_{1m} + \ \tau_M)}\right] \quad \text{_____ (1)}$$

$$\left(\frac{1}{\tau_{ci}}\right) = \left(\frac{1}{\tau_M}\right) + \left(\frac{1}{\tau_R}\right) + \left(\frac{1}{T_{ie}}\right) \qquad i = 1,2 \text{ _____(2)}$$

Loading efficiency (%) =

(Weight of drugloaded/weight of total drug added) x 100 _____ (3)

Drug loading % =

The mass of loaded drug/the mass of initial drug and carrier x 100 _____(4)

The drug loading efficiency and drug loading percentages were **64.0** and **8.35%** respectively.

3.7.2 Phantom study

A phantom study was carried out to determine the relationship between T1 and T2 relaxation times with various concentrations of Fe_3O_4@L-Arg/P NPs. For the phantom preparation, aqueous solutions of NPs (0.5, 0.25, 0.1, 0.05, 0.01, and 0.001 mg mL^{-1}) were prepared and transferred into micro centrifuge tubes (2 mL). Pure water and L-arginine solution (1 mg/mL) were taken as references. An array of micro centrifuge tubes was placed in a plastic container with water for magnetic field homogeneity. The phantom was carefully placed in the center of the head coil.

3.7.3 MRI study

MR imaging was performed at RT using a clinical 1.5 T GE Medical Systems scanner in combination with a 16-channel wrist joint coil. To determine the T1 relaxation time of each concentration, spin-echo (SE) sequences with different repetition times (TR; 100, 200, 400, 600, 800, 1000, 2000, 3000 ms) and an echo time (TE; 15 ms) were performed. The other

imaging parameters were as follows: slice thickness = 7 mm, the field of view (FOV) = 5 x 5 cm, matrix = 320 x 192, flip angle = $90^{o,}$ and imaging time = 1.0 min.

For T2 relaxation time, an SE protocol with the following parameters was used: TR = 3000 ms with TE = 9, 27, 36, 99 ms, and other parameters were the same as above. The signal intensity in arbitrary units (a.u.) for each of the imaging sequences was obtained using Dicom (digital imaging and communication in medicine) Works software v 1.3.5 (Dicom Works, Lyon, France) via locating a circular region of interest (ROI) in the center of each tube (maximum region of interest was considered). Recorded signal intensities were fitted in Excel (Windows 10) using the exponential eq. (5) and (6) to evaluate R1 (1/T1) and R2 (1/T2) relaxation rates, respectively.

$Signal_{SE} = S_0(1- e^{-TR/T1})$ _____(5)

$Signal_{SE} = S_0(e^{-TE/T2})$ _____ (6)

The slopes of R1 and R2 relaxations versus the concentration of the samples were calculated as relaxivity values r_1 and r_2 in Microsoft office 2007.

3.7.4 *In vitro* study design

The cell lines used in the experiment (A431 human epidermoid carcinoma cell line) were purchased from the National Center for Cell Science (Pune, India). Dulbecco's Modified Eagle's Medium (DMEM) with low glucose supplemented with 10% fetal bovine serum (FBS) with 1% antibiotic solution (penicillin and streptomycin) was used for the maintenance and healthy growth of the cells. The cells were cultured in a constant environment at 37 °C with 5% CO_2 in a humidified CO_2 incubator. A wide range of concentrations starting from 1 µg mL^{-1} to 1000 µg mL^{-1} was selected for the in vitro study as in the initial screening, the formulations were found to cause almost complete mortality at higher doses. The range selected was 1, 2, 3, 4, 5, 6, 7, 8, 9, 10, 100, 200, 500, 750, and 1000 µg mL^{-1}. The details of the experiment are described as follows.

3.7.5 *In vitro* drug release kinetics

To study the drug release kinetics, three different experiments were performed (Image 3.1). This study was carried out at 37 ^oC and pH 7.4. In each experiment, 3.0 mg of cloaded magnetic NPs were added to a flask having 30 mL of Na_2HPO_4–NaH_2PO_4 buffer solution. The flask was then kept in a shaker at 37 ^oC. The release medium was withdrawn at predetermined time intervals (1, 2, 3, 4, 5, 6, 7, 8, 9, 12, 24, 36, 48, 60, 80, 100, 124, 148, 172 and 196 h). The collected samples were analyzed using a UV-vis spectrophotometer (Perkin-

Elmer Lambda 35) to determine the amount of Birigatinib released (λ_{max} = 284 nm).

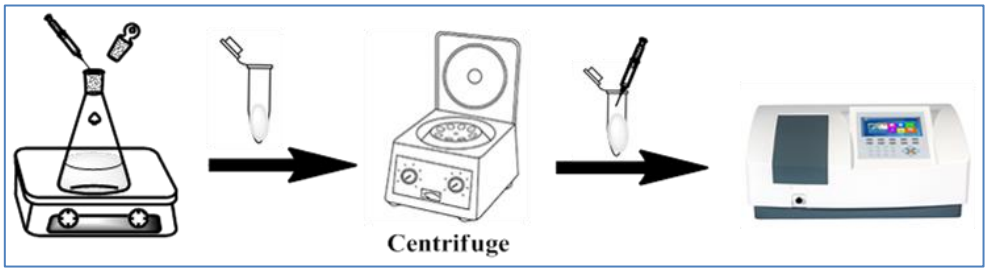

Image 3.1. *In vitro* drug release kinetics process

3.7.6 *In vitro* cytotoxicity test

The cytotoxicity of all the samples was tested on an A431 epidermoid carcinoma cell line by a 3-(4,5-dimethylthiazol-2-yl)-2,5-diphenyltetrazolium bromide (MTT) assay (Sigma-Aldrich, USA). In complete full-growth media, A431 cells were seeded in a 96-well plate (5 x 10^3 cells per well). Then, cells were treated with Fe_3O_4@L-arg NPs, Brigatinib-loaded NPs, and pristine brigatinib of the same amount as loaded on NPs for 48 h at 37 ^oC. After 48 h, the MTT was added to each well and the cells were incubated at 37 ^oC for 4 h. The medium was removed and dimethyl sulfoxide (DMSO) was added to dissolve the formazan crystals. The absorbance was measured at 570 nm with a Microplate Reader (iMark, BioRad, USA). The experiments were performed in triplicate. The relative cell viability (RCV) w.r.t. the control wells were calculated by the following equation:

$RCV = (OD_{test}/OD_{control}) \times 100\%$,

Where, OD_{test} and $OD_{control}$ were obtained in the presence and absence of the NPs, respectively.

3.7.7 Clonogenic assay

We used a clonogenic assay to determine the colony-forming ability of cells under the effect of different treatments. For this assay cells were seeded in 6-well plates at their log phase. A thousand cells per well were plated and incubated in the total media (DMEM low glucose, 10% FBS, 1% antibiotic solution). These were treated with the M^{2+}/ Fe_3O_4@L-Arg/P/bg and bared brigatinib drugs for 48 hours. The medium was then replaced with new media without any added drugs or formulations. Colonies were stained with crystal violet after 5 days of treatment. The number of colonies containing at least 50 cells was counted using the Image J software (NIH, USA). The percentage of colonies formed was calculated by dividing the

number of colonies by a product of the number of cells plated and the plating efficiency. Data were obtained in triplicates and graphs were prepared in GraphPad PRISM software (San Diego, CA, USA).

3.8 References

1. W.Wei, C. Z. Jiang, V. A. L. Roy, Nanoscale. 8, 19421, (2016).
2. E. K. Lim, T. Kim, S. Paik, S. Haam, Y. M. Huh, K. Lee, Chem. Rev. 115, 327, (2015).
3. Z.R. Lu, P. Qiao, Mol Pharmaceutics. 15, 3603 (2018).
4. F. M. Kievit, M. Zhang, Acc. Chem. Res., 44, 853, (2011).
5. M. U. Muckenthaler, S. Rivella, M. W. Hentze, B. Galy, Cell 168 (2017).
6. N. Lee, T. Hyeon, Chem Soc Rev. 41, 2575, (2012).
7. R. C. O'Handley, Wiley-Interscience, NY. (1999).
8. J. W. M. Bulte, D. L. Kraitchman, NMR Biomed. 17, 484, (2004).
9. B. D. Cullity, (Addision Wesley Pub. Co.,USA ,1972) pp 666.
10. Q. A. Pankhurst, J. Connolly, S. K. Jones, J. Dobson, J. Phys. D: Appl. Phys. 36, 167, (2003).
11. U. Jeong, X. Teng, Y. Wang, H. Yang, Y. Xia, Adv. Mater. 19, 33, (2007).
12. D. Ho; X. Sun; S. Sun; Acc. Chem. Res., 44, 875, (2011).
13. Y. S. Kang, S. Risbud, J. F. Rabolt, P. Stroeve, Chem. Mater. 8, 2209, (1996).
14. X. K. Zhao, P. J. Horve, J. H. Fendler, J. Phys. Chem. 93, 908, (1989).
15. J. Cheon, J-H. Lee, Acc. Chem. Res. 2008, 41, 1630, (2008)
16. Y-X. J. Wang, Quant Imaging Med Surg. 1, 3, (2011).
17. F. Kiessling, M. E. Mertens, J. Grimm, T. Lammers, Radiology. 273, 10, (2014).
18. L. Sandiford, A. Phinikaridou, A. Protti, L. K. Meszaros, X. J. Cui, Y. Yan, G. Frodsham, P. A.Williamson, N. Gaddum, R. M. Bottnar, P. J. Blower, M. A. Green, T. M. de Rosales, ACS Nano. 7, 500, (2013).
19. A. Cabrera- Garcia, E. Checa-Chavarria, J. Pacheco-Torres, A. BernabeuSanz, A. Vidal –Moya, E. Rivero- Buceta, G. Sastre, E. Fernandez, P. Botella, Nanoscale. 10, 6349, (2018).
20. C. Tu, E. A. Osborne, A. Y. Louie, Ann. Biomed. Eng. 39, 1335, (2011).
21. F. M. Kievit, M. Zhang; Acc. Chem. Res., 44, 853, (2011).

22. A. Senpan, S.D. Caruthers, I. Rhee, N.A. Mauro, D. Pan,G. Hu ,M.J. Scott, R.W. Fuhrhop , P.J. Gaffney, S.A. Wickline , G.M. Lanza , ACS Nano., 3, 3917, (2009).
23. J. Wahsner, E.M. Gale, A. Rodríguez-Rodríguez, P. Caravan, Chem Rev., 119, 957, (2019).
24. E.A. Schellenberger, A. Jr. Bogdanov, D. Hogemann, J. Tait, R. Weissleder, L. Josephson, Mol. Imaging., 1, 102, (2002).
25. T. Hyeon, Chem Commun., 8, 927, (2003).
26. X. Wang, RD Tilley, J. J. Watkins, Langmuir., 30, 1514, (2014).
27. N. Lee, D. Yoo, D. Ling, M. H. Cho, T. Hyeon, J. Cheon, Chem Rev., 115, 10637, (2015).
28. B.H. Kim, N. Lee, H. Kim, K. An, Y.I. Park, Y. Choi, K. Shin, Y. Lee, S.G. Kwon, H.B. Na, J.G. Park, T.Y. Ahn, Y.W. Kim, W.K. Moon, S.H. Choi, T. Hyeon, J. Am, Chem. Soc., 133,12624, (2011).
29. S. H. Lee, B.H. Kim, H.B. Na, T. Hyeon, Nanomed Nanobiotechnol., 6, 196, (2013).
30. F.L. Deepak, M. Bañobre-López, E. Carbó-Argibay, M.F. Cerqueira, Y. Piñeiro-Redondo, J. Rivas, C.M. Thompson, S. Kamali, C. Rodríguez-Abreu, K. Kovnir, Y.V. Kolen'ko, J Phys Chem C., 119, 11947, (2015).
31. D.A. Benaron, Cancer and Metastasis Rev., 21, 45, (2002).
32. Y. –w. et al. J. AM. CHEM. SOC., 127, 5732, 2005.
33. S. Bedi, S.A. Khan, M.M. AbuKhader, P. Alam, N.A. Siddiqui, A.A. Husain, Saudi Pharm J. 26,755, (2018).
34. M.D. Vincent, M.S. Kuruvilla, N.B. Leighl, S. Kamel–Reid, Curr. Oncol., 19, 33, (2012).
35. C.M. Della Corte, G. Viscardi, R.D. Liello, M. Fasano, E. Martinelli, T. Troiani, F. Ciardiello, F. Morgillo, Mol Cancer., 17, 30, (2018).
36. W.S. Huang, S. Liu, D. Zou, M. Thomas, Y. Wang, T. Zhou, J. Romero, A. Kohlmann, F. Li, J. Qi, L. Cai, T.A. Dwight, Y. Xu, R. Xu, R. Dodd, A. Toms, L. Parillon, X. Lu, R. Anjum, S. Zhang, F. Wang, J. Keats, S.D. Wardwell, Y. Ning, Q. Xu, L.E. Moran, Q.K. Mohemmad, H.G. Jang, T. Clackson, N.I. Narasimhan, V.M. Rivera, X. Zhu, D. Dalgarno, W.C. Shakespeare, J Med Chem. 59, 4948, (2016).
37. E. Shah, A. Kadam, T. Jubin, R. Begum, P. Upadhyay, H.P. Soni, ChemistrySelect., 4, 7883, (2019).
38. E. Shah, P. Upadhyay, M. Singh, M.S. Mansuri, R. Begum, N. Sheth, H.P. Soni, New J. Chem., 40, 9507, (2016).

39. U. Schwertmann, R.M. Cornel, The Iron Oxides. (Wiley-VCH, Weinheim, 2000).
40. S. Xuan,Y.XJ. Wang, J. C. Yu, KC.F. Leung, Chem. Mater., 21, 5079, (2009).
41. E. Shah, H.P. Soni, RSC Adv., 3, 17453, (2013).
42. J. Liu, Y. Bin, M. Matsuo, J. Phys. Chem. C., 116, 134, (2012).
43. S. Kamali-M, A.M. Blixt, L. Haggstrom, R. Wappling, V. Stanciu, P. Nordblad, J Magn Magn Mater., 272, 1263, (2004).
44. K.M. Krishnan, IEEE Trans Magn., 46, 2523, (2010).
45. S. Xuan, Y.XJ. Wang, J. C. Yu, KC.F. Leung, Chem. Mater., 21, 5079, (2009).